ELSEVIER

Contents lists available at ScienceDirect

Extreme Mechanics Letters

journal homepage: www.elsevier.com/locate/eml



The strength of an adhesive contact in the presence of interfacial defects

Coby K. Jones ^a, Jamie L. Hale ^a, Helen K. Minsky ^b, Jamie A. Booth ^{a,*}

- ^a Department of Mechanical Engineering, California State University Northridge, Northridge, CA, USA
- ^b Department of Physics and Astronomy, Carlton College, Northfield, MN, USA

ARTICLE INFO

Dataset link: https://doi.org/10.17632/kwy63t

Keywords:
Adhesion mechanics
Contact
Defects
Cohesive zone modeling
Finite element analysis

ABSTRACT

Adhesive contacts which possess a dominant stress concentration, such as at the contact edge in spherical junctions or at the detachment front in a peeling film, are well studied. More complex adhesive junction geometries, such as mushroom-shaped fibrils in bioinspired micropatterned dry adhesives, have exhibited a complex dependence of adhesive strength on the presence of interfacial defects within the contact. This has led to the emergence of statistical variation of the local behavior among micropatterned sub-contacts. In order to examine the interplay between geometry and interfacial defect character in control of the adhesive strength, the model system of a stiff cylindrical probe on an elastic layer is examined. Both experiments (glass on PDMS) and cohesive zone finite element simulations are performed, with analytical asymptotic limits also considered. The thickness of the elastic layer is varied to alter the interfacial stress distribution, with thinner layers having a reduced edge stress concentration at the expense of increased stress at the contact center. The size and position of manufactured interfacial defects is varied. It is observed that for the thickest substrates the edge stress concentration is dominant, with detachment propagating from this region regardless of the presence of an interfacial defect within the contact. Only very large center defects, with radius greater than half of that of the contact influence the adhesive strength. This transition is in agreement with analytical asymptotic limits. As the substrate is made thinner and the stress distribution changes, a strong decay in adhesive strength with increasing center defect radius emerges. For the thinnest substrate the flaw-insensitive upper bound is approached, suggesting that this decay is dominated by a reduction in the contact area. For penny-shaped defects at increasing radial positions, the adhesive strength for the thinnest substrates becomes non-monotonic. This confirms an intricate interplay between the geometry-controlled interfacial stress distribution and the size and position of interfacial defects in adhesive contacts, which will lead to statistical variation in strength when defects form due to surface roughness, fabrication imperfections, or contaminant particles.

1. Introduction

The geometry of adhesive junctions is known to influence the stress distribution at the interface. This may lead to the nucleation of detachment beginning at the contact edge, such as in spherical contacts [1–3] or in peeling [4–6]. However, the strength of adhesive junctions with more complex geometries may be controlled by pre-existing defects within the interface. This is the case for bioinspired micropatterned adhesives, where arrays of sub-contacts form at the tip of individual fibrils. These junctions may have complex geometries [7–10] or variation of material properties close to the interface [11–14]. Fig. 1(a) illustrates a typical 'mushroom-shaped' fibrillar micropatterned adhesive, and the contact which forms with a target surface [15,16]. Defects in the interface may result from surface roughness, fabrication imperfections, or contaminant particles. One defect may be dominant in controlling detachment, or defects may interact. In either case, variation in the

defect distribution from fibril to fibril leads to local statistical variation in strength across the array. Fig. 1(b) shows the force–displacement characteristics of the separation process, and the progressive detachment of fibrils which results despite assurance of a uniform load distribution among the sub-contacts. Fig. 1(c) shows the distribution in elongation at detachment of individual fibrils, decomposed by the dominant defect type as determined by in-situ contact visualization. This local strength distribution has been shown to influence the global strength and stability of micropatterned adhesive patches [15–17].

In order to understand how this statistical variation emerges, it is necessary to systematically study the strength of an adhesive contact in the presence of defects of specified size and location within the interface. Furthermore, the interplay of the geometry of the adhesive junction with these defects, and their propagation characteristics,

E-mail address: jamie.booth@csun.edu (J.A. Booth).

^{*} Corresponding author.

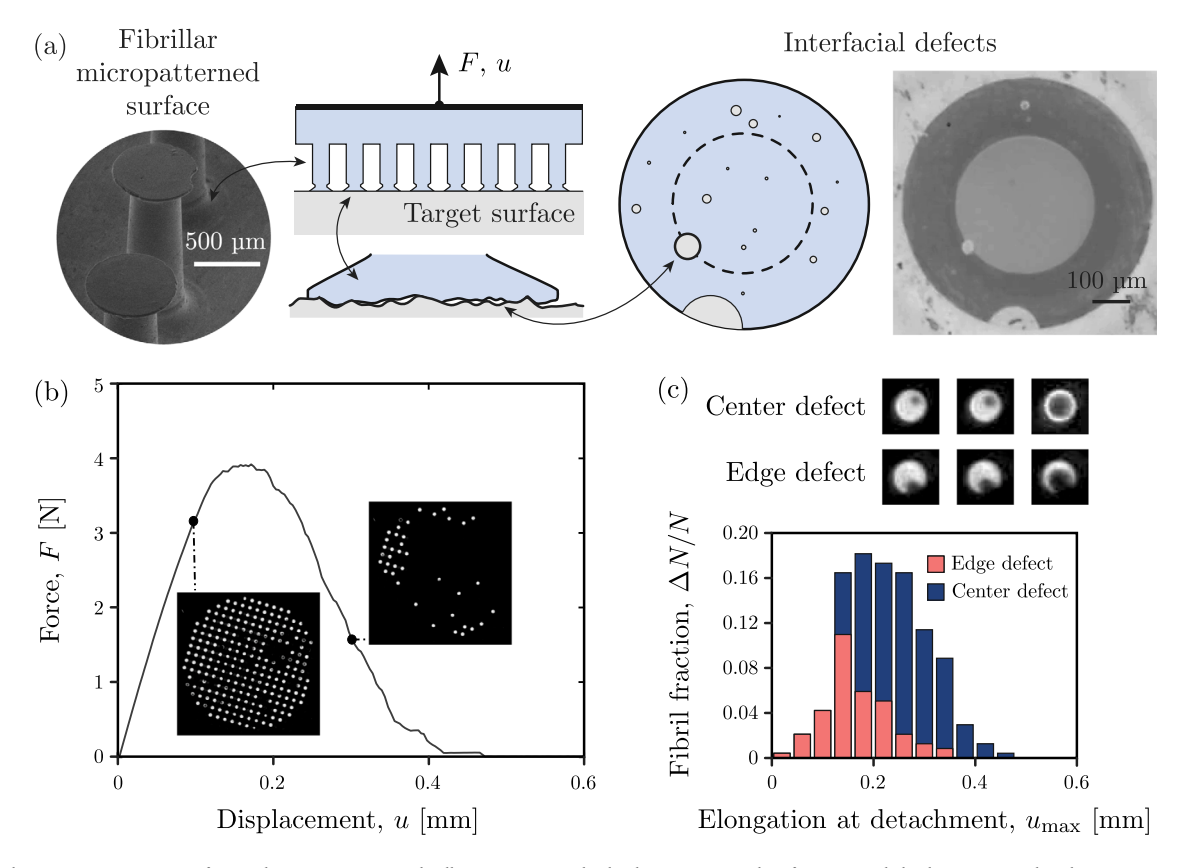


Fig. 1. (a) Schematic representation of a synthetic micropatterned adhesive contact. The loading system applies force *F*, and displacement *u*. Also shown is a scanning electron micrograph of mushroom fibril microstructures as well as a contact image against a rough and contaminated surface that induces multiple interfacial defects at the fibril tip. Adapted from [15] (CC BY license); (b) Tensile load vs. displacement applied to an adhesive joint consisting of an array of micropatterned sub-contacts. Insets show the contact at two points during retraction, demonstrating progressive stochastic detachment of fibrils. Adapted with permission from [16]; (c) Exemplary center and edge defects during propagation, and the histogram of elongation at detachment (representing the local adhesive performance of individual sub-contacts) broken down by defect type. Adapted with permission from [16].

should be examined. This work seeks to achieve this through exploration of a stiff cylindrical punch in contact with a compliant elastic layer, where manufactured defects are created in the punch.

2. Theory

Fig. 2a–b show the geometric and elastic properties of this configuration. The rigid punch is characterized by radius, b, and the elastic layer by thickness, h, Young's modulus, E, and Poisson ratio, v (where henceforth $E^* = E/(1-v^2)$). The adhesive interaction is characterized by the intrinsic strength, σ_0 , and work of adhesion, W. A penny shaped defect of radius, a, is introduced at radial position, p. It is introduced on the rigid punch and is assumed to completely interrupt the adhesive interaction, hence its depth is arbitrary. The junction is subject to a remote applied displacement, Δ , and a corresponding nominal applied stress, σ . The peak applied stress during separation is defined as the adhesive strength, $\sigma_{\rm max}$.

Defect-insensitive detachment refers to the optimal condition in which the adhesive strength is controlled by the intrinsic strength of the interaction across the entire contact [18]. This is a result of the interfacial stress distribution being approximately uniform, which occurs when the length-scale which controls the size of the fracture process zone, E^*W/σ_0^2 , is large in comparison to the dimensions of the contact or the thickness of the layer. Defect-insensitivity may result from a long-range adhesive interaction, or when opening displacements are limited by high modulus. It represents the upper bound on the adhesive strength, which is obtained based on the contact area as

$$\sigma_{\text{max}} = \sigma_0 \left[1 - \left(\frac{a}{b} \right)^2 \right]. \tag{1}$$

Conversely, when the fracture process zone is very small, the linear elastic interfacial stress distribution dominates. In the limit that $h \gg b$, and in the absence of any interfacial defects (a/b=0), the analytical solution for this stress distribution is [19]

$$\sigma_{zz} = \frac{\sigma}{\left[1 - \left(\frac{r}{b}\right)^2\right]^{\frac{1}{2}}}.$$
 (2)

The asymptotic elastic stresses at the contact edge $(r \rightarrow b)$ are singular and equivalent to the tip of a crack in a bulk material, with stress intensity factor

$$K_{\rm I} = \frac{1}{2}\sigma\sqrt{\pi b},\tag{3}$$

leading to the linear elastic fracture mechanics (LEFM) limit of the adhesive strength when controlled by detachment from the contact edge [20]

$$\sigma_{\text{max}} = \left(\frac{8E^*W}{\pi b}\right)^{\frac{1}{2}}.\tag{4}$$

An analytical solution for a center defect is also available in the limit of $h \gg b$, where the stress intensity factor is equivalent to a penny-shaped defect in the center of a rod [21]

$$K_{\rm I} = \frac{2}{\pi} \sigma \sqrt{\pi a} f\left(\frac{a}{b}\right),\tag{5}$$

where

$$f\left(\frac{a}{b}\right) = \frac{1 - 0.5\left(\frac{a}{b}\right) + 0.15\left(\frac{a}{b}\right)^3}{\left[1 - \left(\frac{a}{b}\right)\right]^{\frac{1}{2}}},\tag{6}$$

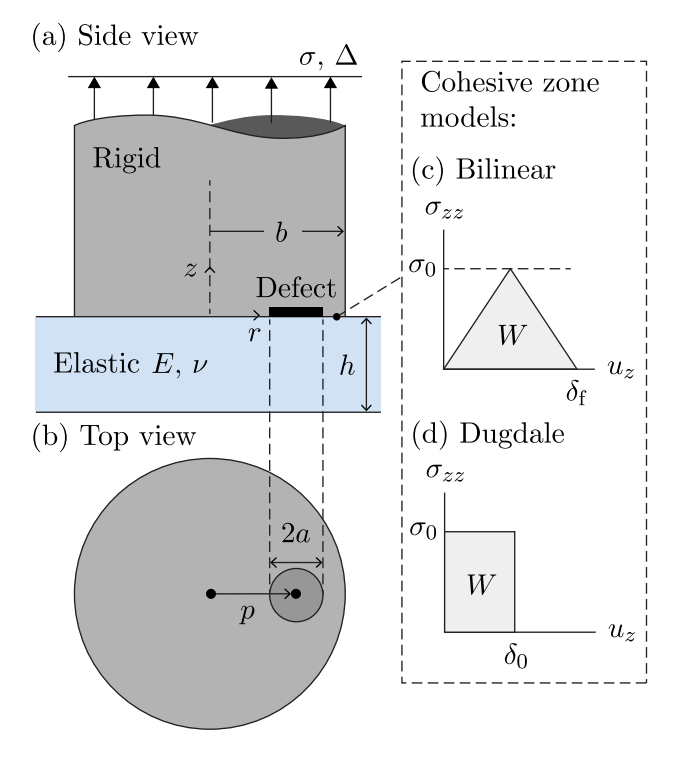


Fig. 2. Schematic of adhesive junction geometry utilized in both modeling and experiment. A glass cylinder contacts a polydimethylsiloxane (PDMS) layer. For the purpose of modeling the glass is treated as rigid and the PDMS as a linear elastic solid. A circular defect is created in the cylinder at a specified radial position. Adhesion is modeled by definition of a cohesive zone traction-separation law at the interface.

leading to the linear elastic fracture mechanics (LEFM) limit of the adhesive strength when controlled by detachment from the defect at contact center

$$\sigma_{\text{max}} = \left(\frac{\pi E^* W}{2af \left(\frac{a}{b}\right)^2}\right)^{\frac{1}{2}}.$$
 (7)

Detachment may be governed by a competition of the center defect and the contact edge, in which case the lesser of the results of Eqs. (4) and (7) will dominate asymptotically. The center defect size associated with transition between regimes is given by solution of the nonlinear equation

$$\frac{a}{b}f\left(\frac{a}{b}\right)^2 = \frac{\pi^2}{16},\tag{8}$$

thus center defects with size exceeding approximately a/b = 0.514 will control detachment. It should be noted that this transition point will change for thinner substrates, where a stress concentration emerges at the contact center, as will be discussed later in this work. The adhesive strength of perfect contacts on thin elastic substrates has previously been considered analytically [20,22–24], by numerical simulation [23, 25], and in experiment [20,22,24]. Here, this treatment is extended to contacts with interfacial defects.

3. Materials and methods

3.1. Experiment

Experiments equivalent to the schematic of Fig. 2 utilize cylindrical glass probes, radius $b=5\,$ mm, on polydimethylsiloxane (PDMS) samples of four different thicknesses, h=[0.5,1.5,3,5] mm. Sylgard 184 (Dow Corning, Midland, MI) is mixed at a 10:1 ratio of base to curing agent. The thinnest sample was spin coated, while the thicker

three are molded. All are cured at a temperature of 85 °C for 4 h. The glass is polished to an optical grade of 60-40 (MIL-REF-13830B). The defects are made by drilling into the glass probe. Center defects of five different sizes, a = [0.815, 1.345, 1.88, 2.285, 2.75] mm, are created. Additionally, a defect of radius a = 1.75 mm is placed at five radial locations, p = [0, 1, 1.5, 2, 2.5] mm, from the center of the probe. The probe and sample are aligned using a custom-built two motor stage, and a Nelder–Mead algorithm is used to adjust the angle to find the peak adhesive force. The adhesion tests are performed on a 2.5 kN zwickiLine tensile tester (ZwickRoell USA, Kennesaw, GA). The probe and sample are brought to a compressive preload of 10 N through approach at a rate of 1 mm/min, followed by a 20 s hold period and a retraction at a rate of 1 mm/min.

3.2. Cohesive zone finite element model

The model shown schematically in Fig. 2a-b is implemented numerically using finite element analysis in ANSYS Mechanical [26]. The radius of the punch is set to unity such that b serves to normalize all length scales. Linear elastic solid elements (PLANE183 for 2D axisymmetric studies and SOLID187 for 3D studies) are utilized to model both the cylindrical punch and the substrate. Results obtained show that largest principal strains observed across all simulations are < 1%, thus the nonlinear elastic response of the elastomer substrate is not expected to play a significant role. A uniform mesh of quadrilateral elements is utilized. The modulus of the substrate is set to unity such that E serves to normalize all parameters of dimension force per unit area. The modulus of the cylindrical punch is set to 10^3 to render its compliance negligible relative to the substrate. The Poisson ratio of both the cylindrical punch and the elastic substrate are set to ν 0.49 to avoid numerical issues associated with incompressibility. A bilinear cohesive zone model, shown in Fig. 2c, is implemented at the interface using CONTA172/TARGE169 elements for 2D axisymmetric studies and CONTA174/TARGE170 elements for 3D studies, implemented with a pure penalty method. The intrinsic strength, σ_0/E , and the critical separation, δ_f/b , are specified. The contact stiffness is determined automatically based upon the properties of the two bodies. Artificial damping is used to stabilize the numerical solution during debonding, and is set to one-tenth of the time step size. The studies are implemented with control of the normalized applied displacement, Δ/b , with a specified finite increment, $d\Delta/b$, to a final displacement value which ensures complete separation of the two bodies. The nominal stress, σ/E , in reaction to this displacement is recorded throughout the separation. Its maximum defines the adhesive strength, σ_{max}/E . Geometric nonlinearity is considered.

In order to benchmark the model, convergence of the adhesive strength must be ensured as the displacement increment, $\mathrm{d}\Delta/b$, and mesh size, d/b are reduced. In order to enable broader parametric studies, a rule-of-thumb is sought for the selection of these parameters which ensures convergence as the intrinsic properties of the interface are varied. We approximate an elastic half space so that the results can later be compared to available analytical solutions [20,27]. The thickness and width of the substrate, relative to the radius of the punch, are two times larger. The bottom surface of the substrate is fixed, and the outer edge is free. Increasing each of these dimensions to four times larger results in only a ~5% change in the adhesive strength (for the converged case of $\sigma_0/E=0.01$ and $\delta_\mathrm{f}/b=0.001$ discussed later).

Fig. S1-S3 of the Supplementary Information show the results of a convergence study for three values of the intrinsic strength, $\sigma_0/E=[0.001,0.01,0.1],$ for a fixed critical separation, $\delta_{\rm f}/b=0.001.$ The effect of increasing the intrinsic strength is to decrease the size of the fracture process zone at the contact edge, which can be approximated based upon the equations of linear elastic fracture mechanics as

$$\frac{r_{\rm p}}{b} = \frac{1}{\pi} \frac{E^* W}{\sigma_0^2 b} = \frac{1}{2\pi} \frac{E^* \delta_{\rm f}}{\sigma_0 b}.$$
 (9)

This has a significant effect on the manner in which the results converge. It is observed that for a small process zone, a smaller mesh size is required but less refinement of the displacement increment is needed. Conversely, when the process zone is large, larger mesh sizes provide converged results but only with greater refinement of the displacement increment. This result follows intuition, as a large fracture process zone leads to a more uniform interfacial stress distribution (thus less mesh refinement is needed to resolve profile) which in turn leads to a more rapid/simultaneous detachment across the contact (thus a smaller displacement increment is needed to determine maximum stress during this process). It is found that convergence within 1% leads to the identification of the following rule-of-thumb for mesh size

$$\frac{d}{b} < \frac{1}{2} \frac{r_{\rm p}}{b},\tag{10}$$

and displacement increment

$$\frac{\mathrm{d}\Delta}{b} < 10^{-7} \frac{b}{r_{\mathrm{p}}}.\tag{11}$$

An analytical solution based upon a Dugdale traction–separation law, shown in Fig. 2d, is available for benchmarking the numerical solution. The adhesive strength is [27]

$$\sigma_{\text{max}} = \frac{2\sigma_0}{\pi} \left(\frac{c}{b}\right)^2 \left[\sqrt{\left(\frac{b}{c}\right)^2 - 1} + \left(\frac{b}{c}\right)^2 \cos^{-1}\left(\frac{c}{b}\right) \right],\tag{12}$$

where the critical lateral extent of the fracture process zone, c, is given by solution of the non-linear equation

$$\frac{E^*W}{\sigma_0^2 b} = \frac{4}{\pi} \left[\frac{c}{b} - 1 + \sqrt{1 - \left(\frac{c}{b}\right)^2} \cos^{-1}\left(\frac{c}{b}\right) \right]. \tag{13}$$

Fig. 3 shows the results of adopting this rule-of-thumb by comparison of the resulting adhesive strength from FEA with the analytical solutions of Eqs. (4) and (12). Equivalence of the fracture process zone size for the Dugdale traction-separation law (analytical) and bilinear traction-separation law (FEA) is ensured by imposing the condition $\delta_{\rm f}=2\delta_{\rm c}$, thus $E^*W/\sigma_0^2b=E^*\delta_{\rm c}/\sigma_0b=E^*\delta_{\rm f}/2\sigma_0b$. Two sets of FEA results are presented. For the first set, the critical separation is held fixed, $\delta_f/b = 0.001$, and the intrinsic strength, σ_0/E , is varied to alter the process zone size. For the second set, the intrinsic strength is held fixed, $\sigma_0/E = 0.01$, and critical separation, δ_f/b , is varied to alter the process zone size. Good agreement is observed between the solutions for process zone sizes smaller than approximately one-tenth of the punch radius. This suggests that in this regime, the normalized strength solution, $\sigma_{\rm max}/\sigma_0,$ is independent of the shape of the traction separation law when the resulting process zone size is equivalent. The FEA results deviate from the analytical solution in the regime of geometry-insensitive detachment. This may be a result of the finite contact stiffness in the FEA solution (i.e. a result of the difference in shape of the traction-separation law), but is not deemed to be a major concern since the focus of this work is defect-controlled detachment, which implies operation outwith this regime. For this reason, the rule-of-thumb is adopted for subsequent studies.

3.3. Extraction of model parameters from experiment

Experiments equivalent to the schematic of Fig. 2 were described in Section 3.1. Results in the absence of a defect (a/b=0) can be utilized to deduce approximate ranges for the interface parameters σ_0/E and δ_f/b to be used in subsequent numerical simulations. The adhesive strength, $\sigma_{\rm max}$, appears to be asymptotically approaching the limit of an elastic half-space as the thickness of the substrate, h, is increased (Fig. S4). Accordingly, it is deemed that a reasonable approximation is obtained when the result from the thickest substrate (h=5 mm) is used in conjunction with the LEFM result of Eq. (4). Adopting an approximation of the modulus, E=2 MPa [28], the strength $\sigma_{\rm max}=32.5 \text{ kPa}$ leads to an estimate of the work of adhesion of $W=0.788 \text{ J/m}^2$.

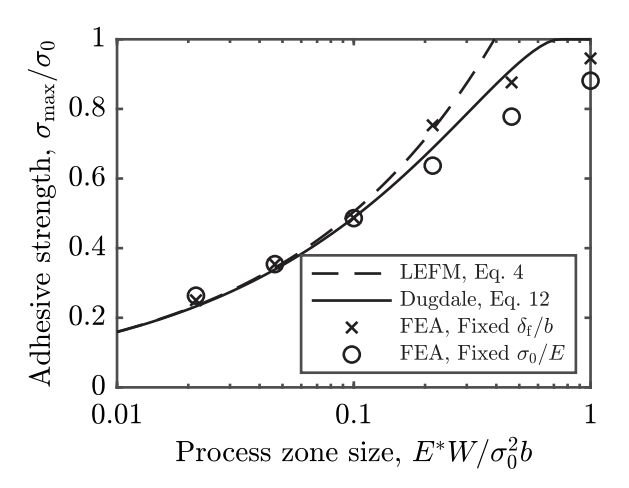


Fig. 3. Normalized adhesive strength, $\sigma_{\rm max}/\sigma_0$ vs. normalized approximate process zone size. Assessment of convergence rule of thumb based upon comparison to analytical models using LEFM (Eq. (4)) and using Dugdale CZM (Eq. (12)). Two sets of FEA results are presented. For the first set (crosses), the critical separation is held fixed, $\delta_I/b = 0.001$, and the intrinsic strength, σ_0/E , is varied to alter the process zone size. For the second set (circles), the intrinsic strength is held fixed, $\sigma_0/E = 0.01$, and critical separation, δ_I/b , is varied to alter the process zone size.

This suggests that the product σ_0/E and $\delta_{\rm f}/b$ should be of order 10^{-4} . Recognizing that the intrinsic strength, σ_0 , will be higher than the largest values of adhesive strength observed for the thinnest substrate with no defect, $\sigma_{\rm max}=142$ kPa, an order of magnitude estimate of intrinsic strength $\sigma_0/E=0.1$ is obtained. Accordingly, for the product to be of order 10^{-4} , the critical separation $\delta_{\rm f}/b=0.001$ is adopted. Given the approximate nature of this parameter selection, for comparison, an order of magnitude lower intrinsic strength, $\sigma_0/E=0.01$, with the same critical separation, $\delta_{\rm f}/b=0.001$, is also considered. It should be noted that this reduction the intrinsic strength should have an equivalent effect to holding the intrinsic strength fixed and increasing the critical separation, as discussed in the previous section.

4. Results and discussion

4.1. Effect of substrate thickness on static stress distribution

Of particular interest in this work is the interplay between the nominal interfacial stress distribution controlled by the global features of the contact geometry, and the presence of defects which perturb this stress distribution locally, in controlling the adhesive strength of the junction. In order to investigate this, the interfacial stress distribution in the absence of a defect is first examined.

Fig. 4 shows the normal stress at the interface, σ_{zz}/σ , where σ is the nominal applied stress. An inverse-square-root singularity is anticipated at the contact edge, as described in Eqs. (2) and (3), and hence a reversed logarithmic scale is used when plotting as a function of the radial position, r/b. Reducing the substrate thickness, h/b, leads to a reduction in the strength of the edge stress concentration, and moves stress toward the contact center. This is the result of a well-known confinement effect, which has been exploited in the design of bioinspired micropatterned adhesive fibrils with soft tip layers [11–14]. In considering the results which follow, this suggests that a different dependence of adhesive strength on defect position may emerge for differing substrate thicknesses.

4.2. Effect of center defect size on strength and propagation characteristics

For the experiments described in Section 3.1, Fig. 5 shows the detachment propagation characteristics and the adhesive strength for preexisting defects located at the contact center as their size is varied.

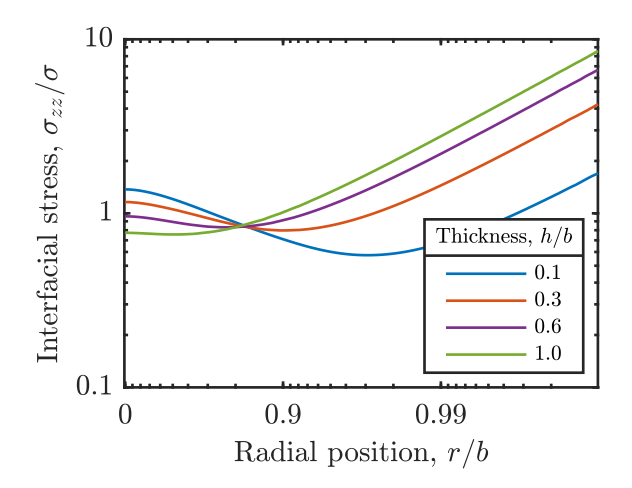


Fig. 4. Normalized interfacial stress, σ_{zz}/σ vs. radial position, r/b. Normalized substrate thickness, h/b, is varied. Note that a reversed logarithmic scale is utilized for the radial position to better visualize the singular result as $r/b \to 1$.

The thickness of the substrate is also varied in order to modify the nominal interfacial stress distribution (Fig. 4). It is observed that for thicker substrates the contact-edge stress-concentration is dominant. Propagation of detachment begins from the contact edge, regardless of the presence of a defect at the contact center (Fig. 5a, h = 5.0 mm). Accordingly, it is observed that the adhesive strength of the junction is approximately independent of the center defect radius in the range examined (Fig. 5b, h = 3.0 mm and h = 5.0 mm). As the thickness of the substrate is reduced, the severity of the edge stress concentration is reduced and the interfacial stress at the contact center increases. It is observed that the detachment propagation changes, and is simultaneously observed from the defect at the contact center and from the contact edge (Fig. 5a, h = 1.5 mm). Accordingly, the adhesive strength decays as the center defect size increases for the two thinner substrates (Fig. 5b, h = 0.5 mm and h = 1.5 mm). The adhesive strength increases as the thickness of the substrate decreases, suggesting that the beneficial effect of reduction of the edge-stress concentration outweighs the detrimental increase in the stress at the contact center (Fig. 4).

These trends can be elucidated by comparison to equivalent simulations. Fig. 6 shows the detachment propagation characteristics and the adhesive strength for preexisting defects located at the contact center as their size is varied. In the contour plots of Fig. 6a the contrast between the punch and substrate indicates separation. The same trends in defect propagation as in experiment are observed, with the thickest substrate being controlled by the edge-stress-concentration and a transition to center-out propagation occurring as the thickness of the substrate is reduced. Fig. 6b also shows equivalent trends in the adhesive strength. An increase in the intrinsic strength of the interface, as shown in Fig. 6c, does not significantly influence the result for the thinnest substrate. Since the primary effect of the increase in intrinsic strength is a reduction in the size of the fracture process zone, this suggests that the thinnest substrate is approaching the limit of flaw-insensitivity. This is confirmed when the results are compared to the upper bound of Eq. (1), which is shown in the dashed lines of Fig. 6b-c. Thicker substrates do exhibit significant differences as the intrinsic strength is varied. The higher intrinsic strength results in a relative reduction in the adhesive strength, as stresses become more localized to the fracture process zone. The difference between the results for the two thickest substrates is reduced, but they have not yet converged as they did in experiment. This suggests the true intrinsic strength of the interface in experiment may be even higher than both cases studied in simulations or, equivalently, the critical separation may be smaller than assumed. The thickest substrates approach the analytical asymptotic limits for the elastic half space identified in Eq. (4) and (7). A gradual transition from edge-controlled to center-controlled detachment is observed close to the transition defect size of a/b = 0.514 identified in Section 2.

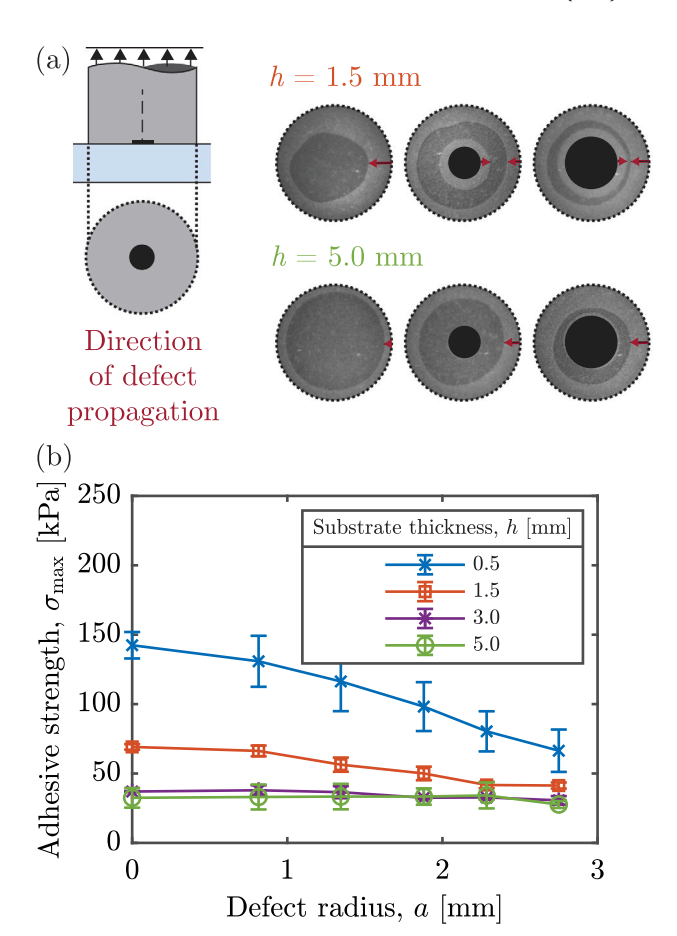


Fig. 5. (a) Experimental detachment propagation characteristics for both a thin (h = 1.5 mm) and thick (h = 5.0 mm) substrate with no preexisting center defect (left) and center defect radii a = 1.345 mm (center) and a = 2.285 mm (right). In each case, the contact image is captured at a time equidistant from the initiation of defect propagation and complete detachment; (b) Adhesive strength, σ_{max} vs. defect radius, a, for a center defect. Substrate thickness, h, is varied.

4.3. Effect of defect location on strength and propagation characteristics

Fig. 7 shows the detachment propagation characteristics and the adhesive strength for preexisting defects at increasing radial positions from the contact center. The thickness of the substrate is once again varied. For the thickest substrate, propagation of detachment begins from the contact edge (Fig. 7a, h = 5.0 mm). This behavior, equivalent to that which was observed for the center defect, persists even as the defect approaches the contact edge (p = 2.5 mm). The adhesive strength remains approximately independent of the center defect radius in the range examined (Fig. 7b, h = 3.0 mm and h = 5.0 mm). As the thickness of the substrate is reduced, a non-monotonic trend emerges. Detachment is simultaneously observed from the defect at the contact center and from the contact edge (Fig. 7a, h = 1.5 mm), as it was for the center defect. The dependence of the adhesive strength on defect position becomes non-monotonic (Fig. 7b, h = 0.5 mm and h = 1.5 mm). In order to explore this trend in more detail, equivalent simulations are performed (Fig. 7c), which additionally allows defect positions up to the contact edge (p/b = 1) to be considered. These simulations are now 3D, due to the breakdown of axisymmetry. The associated computation intensity leads attention to be limited to the thinnest substrate where the non-monotonic trend emerges (h/b = 0.1). It is observed that the strength is lowest when the defect is at the contact center. The strength increases for defects at intermediate positions, and then decays again as the defect reaches the contact edge. This is in

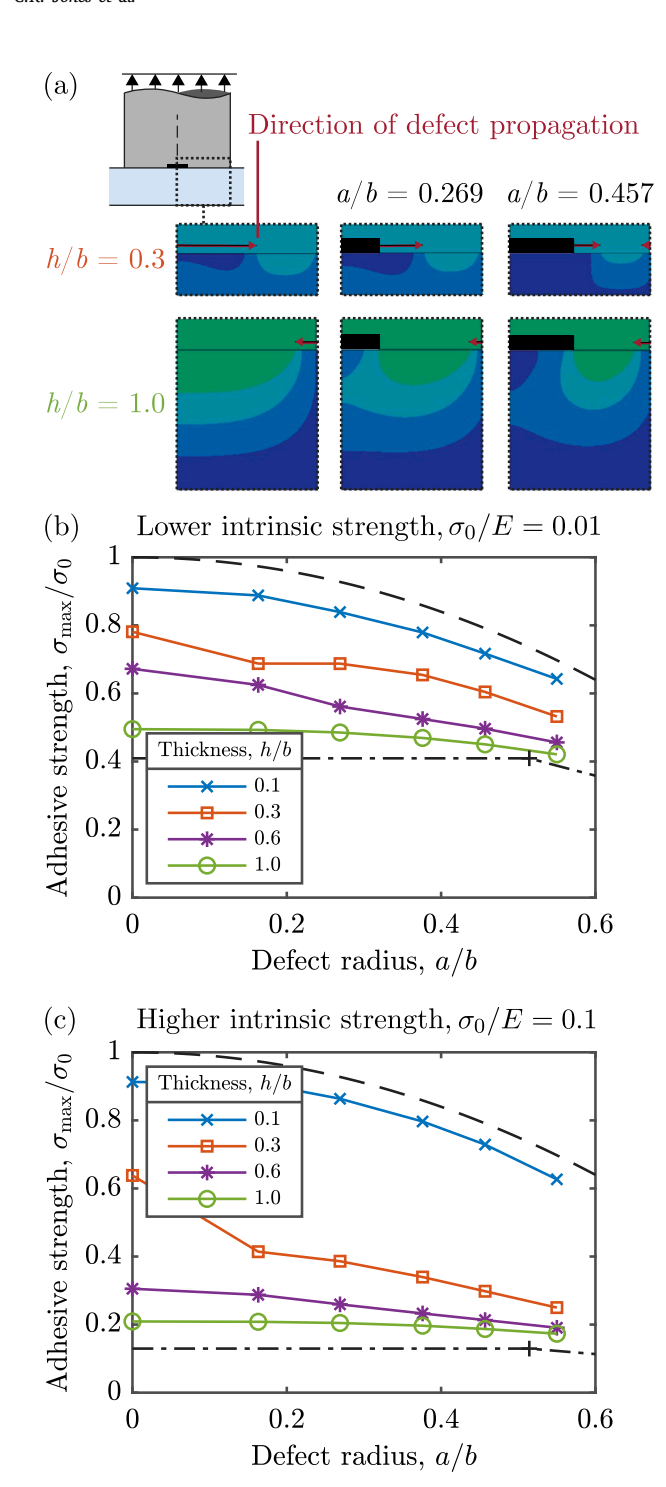


Fig. 6. (a) Simulated detachment propagation characteristics for both a thin (h/b=0.3) and thick (h/b=1.0) substrate with no preexisting center defect (left) and center defect radii a/b=0.269 (center) and a/b=0.457 (right). Results are shown for intrinsic strength $\sigma_0/E=0.01$. Contrast in stress contour color between the rigid punch and the substrate indicates separation. In each case, the image is captured at a displacement equidistant from the initiation of defect propagation and complete detachment; (b)–(c) Normalized adhesive strength, σ_{\max}/σ_0 vs. defect radius, a/b, for a center defect. Normalized substrate thickness, h/b, is varied. Both lower intrinsic strength, (b) $\sigma_0/E=0.01$, and higher intrinsic strength, (c) $\sigma_0/E=0.1$ are compared. The dashed line represents the upper bound associated with defect-insensitive detachment given in Eq. (1), and the dot-dashed line represents the LEFM result in the limit $h\gg b$ with the lower of Eq. (4) for edge-controlled detachment and Eq. (7) for center-defect-controlled detachment being plotted. The + indicates the point of transition between these two regimes. (For interpretation of the references to color in this figure legend, the reader is referred to the web version of this article.)

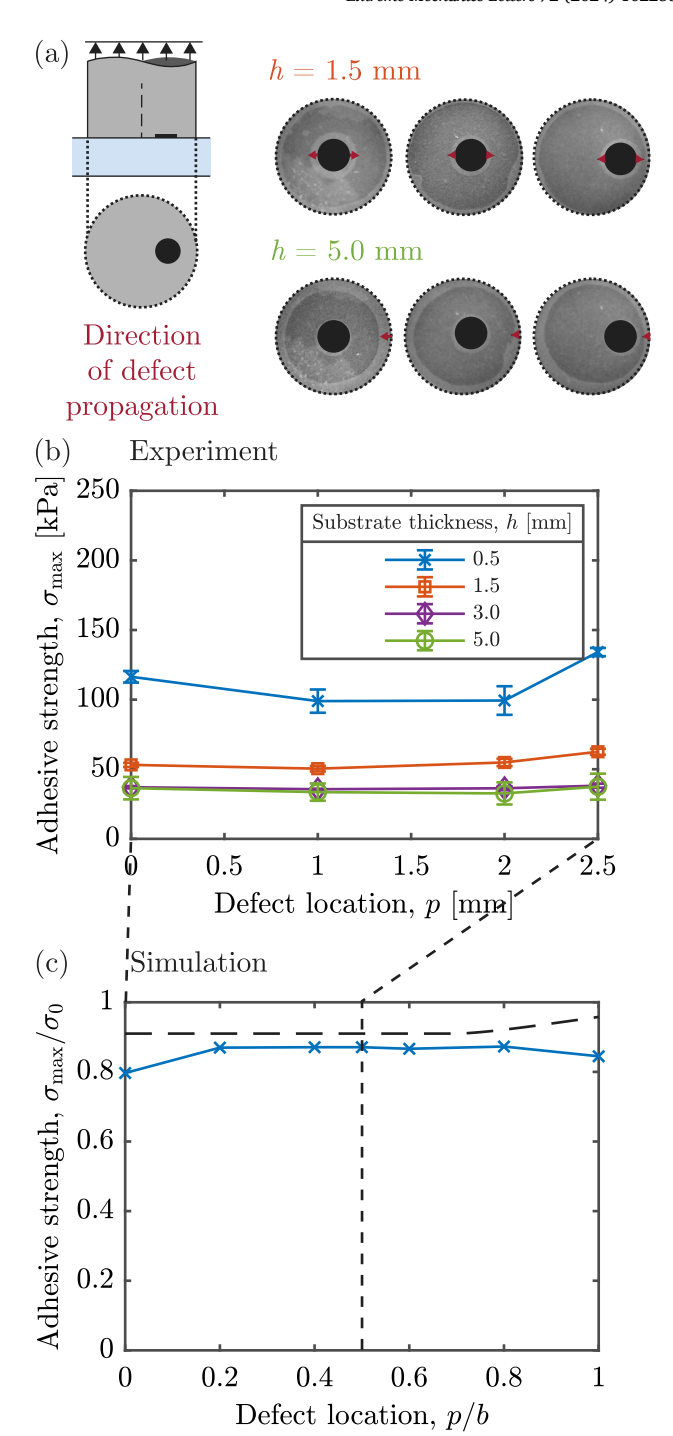


Fig. 7. (a) Experimental detachment propagation characteristics for both a thin ($h=1.5~{\rm mm}$) and thick ($h=5.0~{\rm mm}$) substrate with defect of radius $a=1.75~{\rm mm}$ at increasing radial positions, $p=0~{\rm mm}$ (left), $p=1.0~{\rm mm}$ (center), and $p=2.5~{\rm mm}$ (right). In each case, the contact image is captured at a time equidistant from the initiation of defect propagation and complete detachment; (b) Experimental adhesive strength, $\sigma_{\rm max}$ vs. defect position, p, for a defect of radius $a=1.75~{\rm mm}$. Substrate thickness, h, is varied; (c) Normalized adhesive strength, $\sigma_{\rm max}/\sigma_0$ vs. defect location, p/b, for a penny-shaped defect of normalized radius a/b=0.35. Normalized substrate thickness, h/b=0.1, and intrinsic strength $\sigma_0/E=0.01$. The dashed line represents the upper bound associated with defect-insensitive detachment given in Eq. (1), modified to account for the change in reduction of the contact area as the defect reaches the contact edge.

agreement with the regions of highest stress observed in the nominal interfacial stress distribution (Fig. 4). The reduction in strength for

a defect at the contact edge is further evidence that the behavior is defect-controlled, and the result cannot be explained by the geometry-controlled upper bound shown (Fig. 7c, dashed line). In fact, the upper bound increases as the defect reaches the contact edge as the loss in area is less pronounced. The difference in trend as compared to experiment (Fig. 7b, $h=0.5~\mathrm{mm}$) may be the result of an increased sensitivity to alignment for the thinnest substrates. Nonetheless, this non-monotonic trend highlights the interplay between the geometry-controlled interfacial stress distribution and defect size and location in controlling the strength of an adhesive contact.

5. Conclusions

In this work it has been demonstrated that the dominant singular stress concentration at the edge of an adhesive contact is not always the determinant of adhesive strength. For the model system of a stiff cylindrical punch contacting an elastic substrate of differing thickness. variation in the geometry-controlled interfacial stress distribution can lead to a dependence on interfacial defects within the contact. In thick substrates, the singular stress concentration at the contact edge does render the strength insensitive to the presence of defects at the contact center, except when these defects exceed approximately half of the radius of the contact. This transition was correctly predicted by comparison to analytical models in the limit of an elastic half space. As the thickness of the substrate is reduced, stress increases at the contact center and the strength becomes strongly dependent on defect size at this location. Simulations show that an increase in the intrinsic strength of the interface causes a slower onset of center defect propagation as the thickness is reduced. They also show that the thinnest substrates examined approach the theoretical upper bound associated with the intrinsic strength, where reduction in contact area becomes more significant than defect propagation. Variation in position of defects is also very significant. For the thinnest substrate, it leads to a non-monotonic trend in adhesive strength in accordance with the nominal interfacial stress distribution. Insights from this model adhesive system are relevant to more complex micropatterned surfaces, where variation in strength between sub-contacts emerges due to differences in the local interfacial defect distribution.

Funding

This material is based upon work supported by the National Science Foundation, United States under Grant No. 2211761.

CRediT authorship contribution statement

Coby K. Jones: Visualization, Methodology, Investigation. Jamie L. Hale: Validation, Methodology, Investigation. Helen K. Minsky: Writing – review & editing, Methodology, Investigation, Conceptualization. Jamie A. Booth: Writing – original draft, Visualization, Validation, Supervision, Project administration, Methodology, Funding acquisition, Formal analysis.

Declaration of competing interest

The authors declare that they have no known competing financial interests or personal relationships that could have appeared to influence the work reported in this paper.

Data availability

The data that support the findings of this study are available from the repository at https://doi.org/10.17632/kwy63t55j7.1.

Appendix A. Supplementary data

Supplementary material related to this article can be found online at https://doi.org/10.1016/j.eml.2024.102238.

References

- K.L. Johnson, K. Kendall, A.D. Roberts, D. Tabor, Surface energy and the contact of elastic solids, Proc. R. Soc. A 324 (1558) (1971) 301–313.
- [2] B. Derjaguin, V. Muller, Y. Toporov, Effect of contact deformations on the adhesion of particles, J. Colloid Interface Sci. 53 (2) (1975) 314–326.
- [3] D. Maugis, Adhesion of spheres: The JKR-DMT transition using a dugdale model, J. Colloid Interface Sci. 150 (1) (1992) 243–269.
- [4] K. Kendall, Thin-film peeling-the elastic term, J. Phys. D: Appl. Phys. 8 (13) (1975) 1449.
- [5] M. Thouless, Q. Yang, A parametric study of the peel test, Int. J. Adhes. Adhes. 28 (4) (2008) 176–184.
- [6] P. Gialamas, B. Völker, R.R. Collino, M.R. Begley, R.M. McMeeking, Peeling of an elastic membrane tape adhered to a substrate by a uniform cohesive traction, Int. J. Solids Struct. 51 (18) (2014) 3003–3011.
- [7] A. Del Campo, C. Greiner, E. Arzt, Contact shape controls adhesion of bioinspired fibrillar surfaces, Langmuir 23 (20) (2007) 10235–10243.
- [8] A.V. Spuskanyuk, R.M. McMeeking, V.S. Deshpande, E. Arzt, The effect of shape on the adhesion of fibrillar surfaces, Acta Biomater. 4 (6) (2008) 1669–1676.
- [9] R.G. Balijepalli, M.R. Begley, N.A. Fleck, R.M. McMeeking, E. Arzt, Numerical simulation of the edge stress singularity and the adhesion strength for compliant mushroom fibrils adhered to rigid substrates, Int. J. Solids Struct. 85–86 (2016) 160–171
- [10] S.C.L. Fischer, K. Groß, O. Torrents Abad, M.M. Becker, E. Park, R. Hensel, E. Arzt, Funnel-shaped microstructures for strong reversible adhesion, Adv. Mater. Interfaces 4 (20) (2017) 1700292.
- [11] H.K. Minsky, K.T. Turner, Achieving enhanced and tunable adhesion via composite posts, Appl. Phys. Lett. 106 (20) (2015).
- [12] H.K. Minsky, K.T. Turner, Composite microposts with high dry adhesion strength, ACS Appl. Mater. Interfaces 9 (21) (2017) 18322–18327.
- [13] R.G. Balijepalli, S.C. Fischer, R. Hensel, R.M. McMeeking, E. Arzt, Numerical study of adhesion enhancement by composite fibrils with soft tip layers, J. Mech. Phys. Solids 99 (2017) 357–378.
- [14] S.C. Fischer, E. Arzt, R. Hensel, Composite pillars with a tunable interface for adhesion to rough substrates, ACS Appl. Mater. Interfaces 9 (1) (2017) 1036–1044.
- [15] J.A. Booth, R. Hensel, Perspective on statistical effects in the adhesion of micropatterned surfaces, Appl. Phys. Lett. 119 (23) (2021) 230502.
- [16] J.A. Booth, V. Tinnemann, R. Hensel, E. Arzt, R.M. McMeeking, K.L. Foster, Statistical properties of defect-dependent detachment strength in bioinspired dry adhesives, J. R. Soc. Interface 16 (156) (2019) 20190239.
- [17] R. Hensel, J. Thiemecke, J.A. Booth, Preventing catastrophic failure of microfibrillar adhesives in compliant systems based on statistical analysis of adhesive strength, ACS Appl. Mater. Interfaces 13 (16) (2021) 19422–19429.
- [18] H. Gao, H. Yao, Shape insensitive optimal adhesion of nanoscale fibrillar structures. Proc. Natl. Acad. Sci. 101 (21) (2004) 7851–7856.
- [19] K.L. Johnson, Contact Mechanics, Cambridge University Press, 1987.
- [20] K. Kendall, The adhesion and surface energy of elastic solids, J. Phys. D: Appl. Phys. 4 (8) (1971) 1186–1195.
- [21] H. Tada, P.C. Paris, G.R. Irwin, The Stress Analysis of Cracks Handbook, ASME Press, 2000.
- [22] K.R. Shull, D. Ahn, W.-L. Chen, C.M. Flanigan, A.J. Crosby, Axisymmetric adhesion tests of soft materials, Macromol. Chem. Phys. 199 (4) (1998) 489–511.
- [23] T. Tang, A. Jagota, M.K. Chaudhury, C.-Y. Hui, Thermal fluctuations limit the adhesive strength of compliant solids, J. Adhes. 82 (7) (2006) 671–696.
- [24] S. Choi, S. Lee, Y.-Y. Earmme, Measurement of time-dependent adhesion between a polymer film and a flat indenter tip, J. Phys. D: Appl. Phys. 41 (7) (2008) 074023.
- [25] B. Peng, X.-Q. Feng, Q. Li, Decohesion of a rigid flat punch from an elastic layer of finite thickness, J. Mech. Phys. Solids 139 (2020) 103937.
- [26] ANSYS Contact Technology Guide, ANSYS, Inc., Canonsburg, PA, 2022.
- [27] C.-Y. Hui, N. Glassmaker, T. Tang, A. Jagota, Design of biomimetic fibrillar interfaces: 2. Mechanics of enhanced adhesion, J. R. Soc. Interface 1 (1) (2004) 35–48.
- [28] I.D. Johnston, D.K. McCluskey, C.K. Tan, M.C. Tracey, Mechanical characterization of bulk sylgard 184 for microfluidics and microengineering, J. Micromech. Microeng. 24 (3) (2014) 035017.